Frontiers in Bioscience Landmark

Front. Biosci. (Landmark Ed) **2025**; 30(7): 39722
https://doi.org/10.31083/FBL39722

Original Research

Potassium Clearance in Optic Nerve: A Multidomain Model

Shanfeng Xiao[1], Huaxiong Huang[2,3], Robert Eisenberg[4], Zilong Song[5], Shixin Xu[2,*]

[1]School of Mathematical Sciences, Soochow University, 215006 Suzhou, Jiangsu, China
[2]Zu Chongzhi Center, Duke Kunshan University, 215316 Kunshan, Jiangsu, China
[3]Department of Mathematics and Statistics, York University, Toronto, ON M3J 1P3, Canada
[4]Department of Applied Mathematics, Illinois Institute of Technology, Chicago, IL 60616, USA
[5]Math and Statistics Department, Utah State University, Old Main Hill, Logan, UT 84322, USA
*Correspondence: shixin.xu@dukekunshan.edu.cn (Shixin Xu)

Academic Editor: Graham Pawelec
Submitted: 14 April 2025 Revised: 14 June 2025 Accepted: 27 June 2025 Published: 28 July 2025

Abstract

Background: Ion and water transport in the central nervous system (CNS) is governed by tightly coupled mechanisms involving electrodiffusion, osmotic pressure, and fluid convection. Disruptions to these processes are implicated in pathological conditions. Understanding the coordinated roles of glial cells and perivascular spaces in regulating ionic and fluid homeostasis is essential for interpreting neural function and dysfunction. **Methods**: We developed a multicompartment model of the optic nerve incorporating axons, glial cells, extracellular space (ECS), and three perivascular compartments (arterial, venous, and capillary-associated). The model integrates electrodiffusion of ions, osmotic water transport, and convection, while enforcing electroneutrality and compartmental volume conservation. Numerical simulations were performed using a finite volume method under axisymmetric geometry, and parameter sensitivity was explored through variations in glial membrane conductance, connexin permeability, and aquaporin-4 (AQP4) expression. **Results**: The simulations reveal that potassium released from axons during stimulation is cleared via glial uptake and redistributed through electric drift within glial syncytia. The perivascular pathway provides a secondary route for potassium and water clearance. Decreased glial conductance leads to abnormal firing in unstimulated axons, mimicking epileptiform activity, while reduced connexin coupling increases dependence on perivascular drainage. Changes in AQP4 expression had limited effect on ionic homeostasis in the current model. **Conclusions**: This model provides a biophysically consistent framework to study ionic-fluid coupling in CNS microcirculation. It demonstrates how glial and perivascular compartments cooperate to maintain extracellular potassium balance. The findings offer insight into the mechanisms underlying pathological K^+ accumulation and suggest potential therapeutic targets involving glial modulation and perivascular enhancement. The framework is extensible to other brain regions and conditions involving impaired clearance or excitability.

Keywords: potassium; glial cells; ion transport; water-electrolyte balance; mircociruclation modeling

1. Introduction

Potassium clearance plays a pivotal role in maintaining the stability and functionality of the central nervous system (CNS) [1]. In the resting state, nerve cells maintain a polarized membrane potential, with the interior of the cell negatively charged relative to the outside. This polarization arises from the unequal distribution of key ions—primarily Na^+, K^+, and Cl^-—across the cell membrane, as well as the selective permeability of ion channels and the action of ion pumps. During an action potential, depolarization occurs when voltage-gated Na^+ channels open, allowing a rapid influx of Na^+ ions into the cell. This inward positive current reduces the membrane potential difference, bringing it toward or above zero. Subsequently, voltage-ated K^+ channels open. Repolarization is primarily driven by the efflux of K^+ ions through potassium channels, which restores the negative internal potential. Cl^- ions, depending on their electrochemical gradient, may also contribute to membrane hyperpolarization by moving inward and counteracting depolarization. Proper potassium regulation is critical for stabilizing neuronal membrane potentials, enabling action potential generation and synaptic transmission. During heightened neuronal activity, potassium ions (K^+) are released into the extracellular space (ECS). Without timely clearance, this excess potassium can accumulate, causing pathological depolarization, neuronal hyperexcitability, and potentially trigger seizures.

Glial cells, particularly astrocytes, are essential for potassium clearance in the CNS, including the optic nerve [2]. Through connexin-based gap junctions, astrocytes form a syncytium that facilitates the redistribution and buffering of potassium ions within the ECS [3]. This process is closely coupled to fluid flow within the glymphatic system, where aquaporin-4 (AQP4) channels in astrocytic endfeet regulate water movement [4,5]. The glymphatic system enables cerebrospinal fluid (CSF) influx through perivascular spaces (PVS), facilitating the clearance of metabolic waste products such as amyloid-β, which are implicated in neurodegenerative diseases such as Alzheimer's and cerebral amyloid angiopathy [6–8]. Recent studies have demonstrated that CSF entering the brain via arterial PVS drives solute clearance downstream, a mechanism crucial for maintaining ionic homeostasis and preventing toxic buildup [9,10].

The optic nerve, as part of the CNS, shares structural similarities with the brain, including its narrow ECS and surrounding glial cells [11]. It consists of four regions: the intraocular nerve head, intraorbital, intracanalicular, and intracranial regions [12]. This study focuses on the intraorbital region, which constitutes the majority of the optic nerve. CSF enters the optic nerve through perivascular spaces surrounding blood vessels, interacting with glial cells lining these spaces [13]. This dynamic flow is essential for potassium clearance and waste removal, processes that, when impaired, are associated with conditions such as glaucoma [14].

Mathematical models have been developed to study potassium clearance and spatial buffering, focusing primarily on fluid dynamics and ionic transport. Early models examined fluid flow within the perivascular spaces, often driven by arterial pulsations [15,16]. More recently, machine learning approaches have been employed to explore mechanisms in the glymphatic system [17,18], as comprehensively reviewed in [19]. However, these models exhibit notable limitations. They often neglect the complex interaction between different compartments—such as the ECS, glial cells, and perivascular spaces—and fail to incorporate critical processes such as electric drift and osmotic effects. Electric drift redistributes potassium ions along electrochemical gradients within the glial compartment [20], while osmotic pressure drives water movement in response to ion concentration changes, maintaining ECS volume and astrocyte function [21]. Collectively, these mechanisms ensure efficient potassium clearance and prevent pathological K^+ accumulation, which can otherwise lead to hyperexcitability, excitotoxicity, and cerebral edema formation.

To address these gaps, we developed a multidomain mathematical model that integrates six compartments: axons, glial cells, the extracellular space, and three perivascular spaces (PVS A, V, and C). Building upon the tridomain framework introduced by Zhu *et al*. [22], our model integrates the interplay between ionic electrodiffusion, osmosis, and fluid circulation. By incorporating the dynamics of glial function and glymphatic pathways, this model provides a comprehensive framework for elucidating potassium clearance mechanisms in the optic nerve.

Additionally, our model considers the interaction between the optic nerve and surrounding cerebrospinal fluid, which flows through the perivascular spaces and subarachnoid space (SAS) as part of the glymphatic pathway [23]. By differentiating between extracellular and perivascular spaces and accounting for direct communication between CSF and PVS A and V, we aim to enhance our understanding of glymphatic function in response to neural activity and potassium clearance.

Despite its advancements, the current model has limitations. It assumes spatial homogeneity in the glial compartment and perivascular spaces, neglecting regional variations in permeability, conductivity, and ionic gradients. Furthermore, the simplified representation of potassium channels does not capture the diversity of channel subtypes and their biophysical properties. Additionally, biochemical processes such as enzyme activity and metabolite interactions, which may influence waste clearance, remain excluded. Future refinements addressing these limitations will enhance the model's predictive capacity and applicability to pathological conditions such as neurodegeneration.

The remainder of this article is organized as follows: Section 2 describes the mathematical model for potassium and fluid microcirculation in the optic nerve. Section 3 presents simulation results, focusing on the effects of glial cells and perivascular spaces on potassium clearance. Finally, Section 4 provides concluding remarks and discusses directions for future work.

2. Materials and Methods

Mathematical Model for Microcirculation in the Optic Nerve

Fig. 1 shows the structure we are modeling. This is a subset of all the structures of interest in the optic nerve, but it is a good place to start. Computational domain Ωconsists of the subarachnoid space (SAS) region Ω_{SAS} and optic nerve region Ω_{OP}, i.e.,

$$\Omega = \Omega_{OP} \cup \Omega_{SAS}, \Omega_{OP} \cap \Omega_{SAS} = \Gamma_7,$$

where the domain Ω_{SAS} is filled with CSF, enclosed by dura mater Γ_7 and pia mater Γ_4.

For the optic nerve region, based on the model first proposed in Ref. [22], we introduce a six-domain model for microcirculation of the optic nerve, which is summarized in Table 1. We must remind the reader that the optic nerve bundler contains many nerve fibers, at least one blood vessel, and a glial syncytium as shown in Fig. 1. In addition to the axon (Ω_{ax}), glial (Ω_{gl}), and extracellular (Ω_{ex}) compartments, the model incorporates three perivascular spaces: perivascular space A (surrounding the artery, Ω_{pa}), perivascular space V (surrounding the vein, Ω_{pv}), and perivascular space C (surrounding the capillary, Ω_{pc}), see Fig. 2.

$$\Omega_{OP} = \Omega_{ax} \cup \Omega_{gl} \cup \Omega_{ex} \cup \Omega_{pa} \cup \Omega_{pv} \cup \Omega_{pc}.$$

We apply compartmental mass conservation laws to describe the dynamics of ions and water within and across cellular and extracellular domains. These laws ensure that the model respects fundamental physical principles—such as the conservation of mass and charge—and establish a robust foundation for physiologically realistic and numerically stable simulations. Specifically, the model is derived from ion and fluid conservation laws governing transmembrane transport between intracellular compartments and the ECS, following the framework introduced in [24]. These

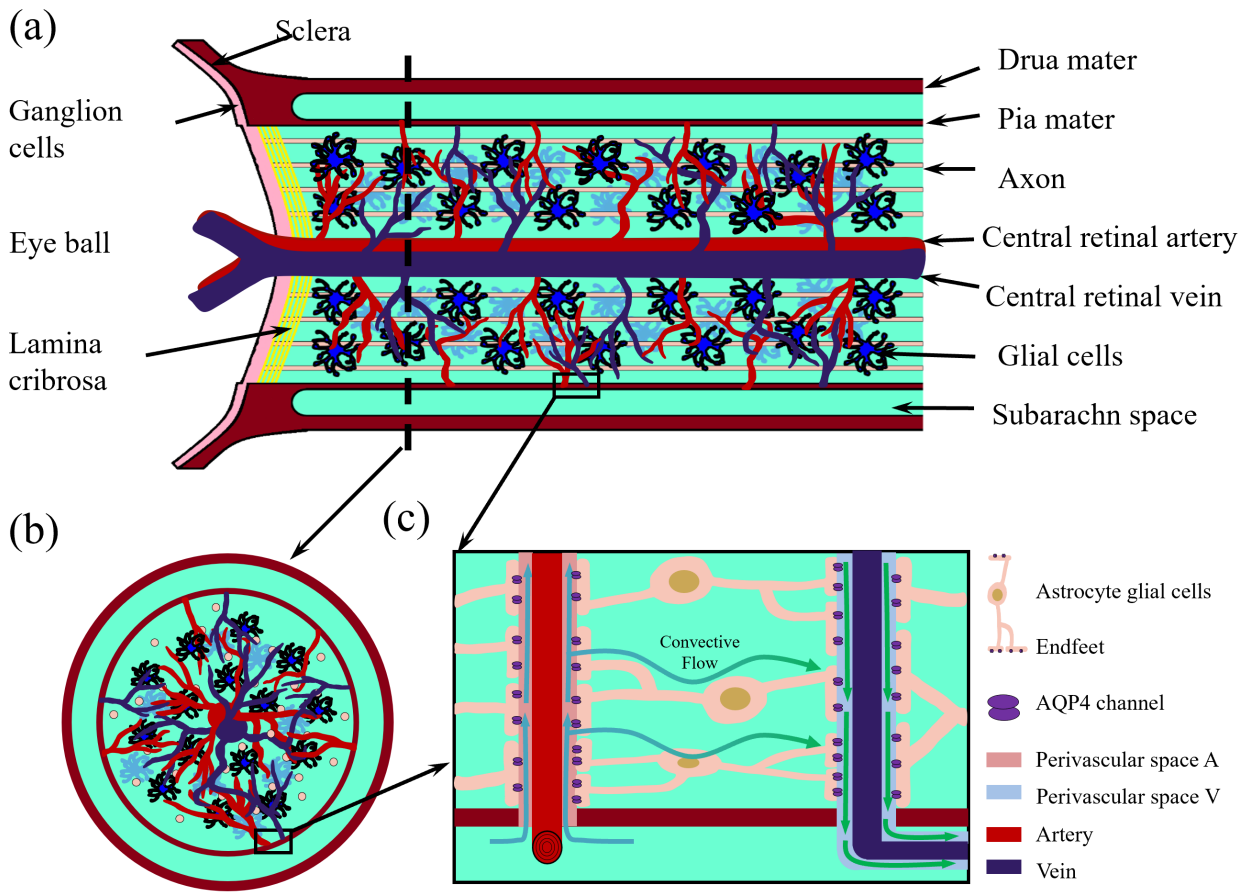

Fig. 1. Optic nerve structure. (a) Longitudinal section of the optic nerve; (b) cross section of the optic nerve; (c) Local zoom in of the glymphatic system. This figure was drawn using MATLAB (R2023b, MathWorks, Inc., Natick, MA, USA).

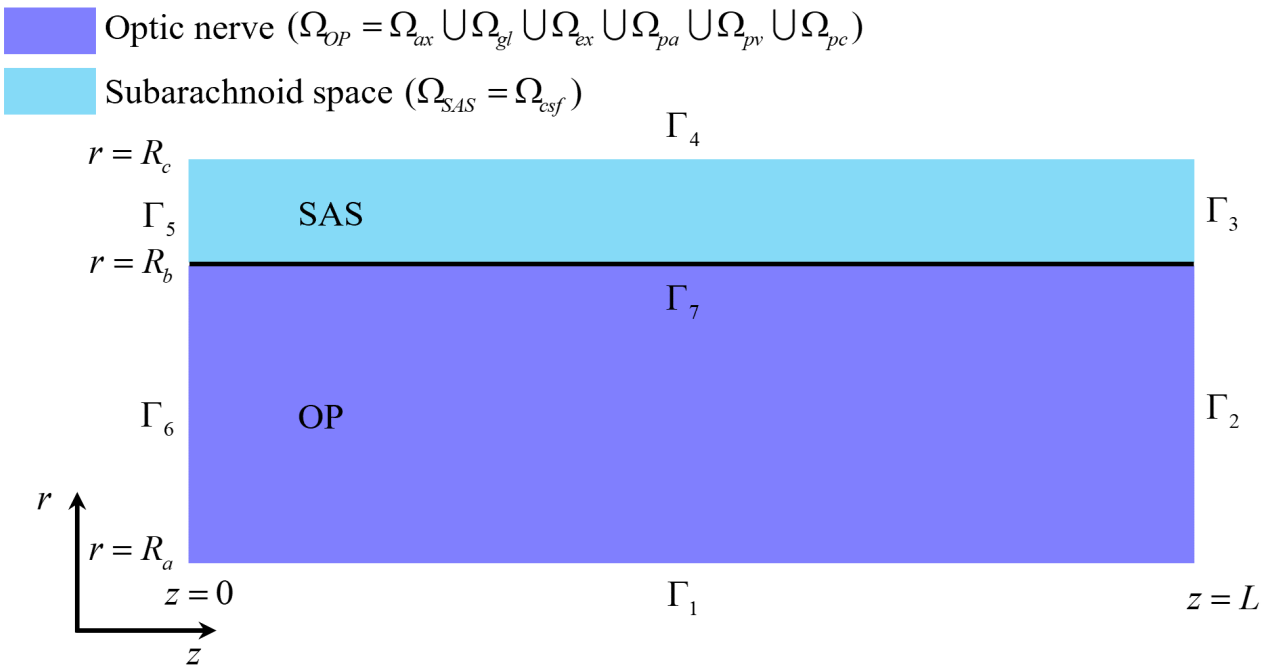

Fig. 2. The optic nerve Ω_{OP} consists of axon compartment, glial compartment, extracellular space, perivascular space. The subarachnoid space Ω_{SAS} only has cerebrospinal fluid. This figure was drawn using MATLAB (R2023b, MathWorks, Inc., Natick, MA, USA). SAS, subarachnoid space; OP, optic nerve.

Table 1. Compartments.

Compartment	Abbreviation	Subscription in formula
extracellular space	ECS	*ex*
perivascular space A	pvsA	*pa*
perivascular space C	pvsC	*pc*
perivascular space V	pvsV	*pv*
cerebrospinal fluid	CSF	*csf*
axon compartment	*ax*	*ax*
glial compartment	*gl*	*gl*

ECS, extracellular space; CSF, cerebrospinal fluid.

conservation principles are applied in each of the six domains: Ω_l, $l = ax, gl, ex, pa, pv, pc$.

$$\frac{\partial}{\partial t}(\eta_l f_l) + \nabla \cdot (\eta_l \boldsymbol{J}_l) + S = 0$$

where η_l is the volume fraction of l compartment, f_l is the concentration of a given substance, $\boldsymbol{J}_l$ is the flux inside the compartment, and S is the source term induced by transmembrane communications due to the active pumps and passive leak channels on the membranes.

For the boundaries, Γ_1 is the central retinal blood wall of the optic nerve; Γ_2 and Γ_3 are the far end (away from the eyeball) of the optic nerve which is connected to optic canal region [25]. Γ_5 is used to model the dura mater connected to the sclera (the white matter of the eye) and assumed to be non-permeable [12]. Γ_6 is used to denote the lamina cribrosa where the optic nerve head exits the eye posteriorly through pores of the lamina cribrosa [26]. We adopt membrane-type boundary conditions to model transmembrane fluxes and compartmental interactions. This choice is motivated by the anatomical context: the intraorbital segment of the optic nerve is embedded in and interacts with surrounding tissues rather than existing in isolation. The membrane boundary conditions allow us to incorporate physiological coupling with adjacent structures, and any region-specific properties (e.g., diffusivity, permeability) can be tuned via coefficients without altering the core model. Additional technical details regarding the boundary condition implementation are provided in the **Supplementary material**.

In this model, the electric potential ϕ_l within each compartment Ω_l is not externally imposed but emerges from the redistribution of mobile ions during neuronal activation. When potassium ions efflux from stimulated axons into the ECS, they cause a local accumulation of positive charge. To restore ionic balance, these ions are subsequently taken up by neighboring glial cells, leading to regional shifts in intracellular electric potential. This spatial potential difference generates an electric field that further drives ionic electrodiffusion within and across compartments.

Rather than solving the Poisson equation for ϕ_l, we adopt a macroscopic electroneutrality assumption, which is valid at tissue scale due to the extremely short Debye length in biological media. Under this assumption, charge separation is negligible compared to the domain size, and the electric potential is determined implicitly by enforcing charge neutrality in each compartment, combined with ionic flux dynamics. This approach is widely used in tissue-level models of electrodiffusion and has the advantage of avoiding the numerical stiffness associated with solving elliptic equations for the electric field. Mathematically, the formulation of electric potential under electroneutrality constraints is provided in **Supplementary material**, where ϕ_l is recovered from ionic concentrations via an algebraic closure condition derived from the ion flux equations. To ensure consistency, we apply homogeneous Neumann boundary conditions for the electric potential on the domain boundaries implying no external electric field enters or leaves the system. This setup isolates the modeled domain electrically and ensures that all electric fields arise from internal biophysical processes, such as ionic imbalance and transmembrane fluxes, consistent with volume conductor theory in neuroscience.

Based on the structure of the optic nerve, we have the following global assumptions for the model (Table 1).

• Axial symmetry: For simplicity, axial symmetry is assumed. To clarify, the model is fundamentally three-dimensional. When axial symmetry is assumed—as in our current implementation—it simplifies the numerical computation without altering the underlying physics. Importantly, the model formulation itself does not rely on symmetry assumptions and can be extended to fully three-dimensional, non-axisymmetric geometries to accommodate spatial heterogeneity or more anatomically realistic structures.

• Ions type: To focus on the primary mechanisms of ionic homeostasis and fluid–ion interaction, the model includes only three major ion species: sodium (Na^+), potassium (K^+), and chloride (Cl^-). These ions are the principal contributors to transmembrane potential, osmotic gradients, and electrochemical fluxes under typical physiological conditions. We acknowledge that other ions and metabolites—such as calcium (Ca^{2+}), protons (H^+), lactate, and glutamate—also play important roles in central nervous system function, particularly in regulating excitability, pH balance, and neuro-glial signaling. However, these species are not included in the current model in or-

der to maintain computational tractability and focus on the dominant components involved in potassium buffering and clearance.

• Charge neutrality: In each domain, we assume electroneutrality [27],

$$\eta_{gl} \sum_i z^i C^i_{gl} + z^{gl} \eta^{re}_{gl} A_{gl} = 0$$

$$\eta_{ax} \sum_i z^i C^i_{ax} + z^{ax} \eta^{re}_{ax} A_{ax} = 0$$

$$\sum_i z^i C^i_l = 0,\ l = ex,\ pa,\ pv,\ pc,\ csf,$$

where $A_l > 0$ with $l = ax,\ gl$ is the density of proteins in axons or glial cells. Most CNS proteins—such as albumin—have isoelectric points (pI) well below the physiological pH of CSF, which is approximately 7.3–7.4. At this pH, these proteins exist predominantly in their deprotonated form and therefore carry a net negative charge. This property is a general consequence of the amino acid composition of these proteins, where acidic residues (e.g., glutamate and aspartate) contribute to the lower pI values. In our model, we incorporate this biochemical reality by assuming that these negatively charged proteins are permanently distributed within axonal and glial compartments, with an effective valence $z^l = -1, l = ax, gl$. The η_{ax} and η_{gl} are the volume fraction of axon and glial compartments in the optic nerve and η^{re}_{gl} and η^{re}_{ax} are the resting state volume fractions. Under physiological conditions, the extracellular fluid—such as CSF and interstitial fluid—maintains macroscopic electroneutrality, meaning the total concentrations of positive and negative charges are balanced. While transient microscopic charge separations occur (e.g., across the membrane during action potentials), the tissue-scale charge density remains effectively zero, minimizing the risk of unbalanced electrostatic fields. This assumption not only reflects physiological reality but also circumvents the numerical complexity of solving the full Poisson equation, thus enhancing computational efficiency without sacrificing model fidelity.

• Anisotropy of axon compartment and isotropy of other compartments: The axons are separated, more or less parallel cylindrical cells that form separate compartments. They are electrically isolated and molecules cannot diffuse directly from one to another. As a result, the intra-compartment flux of ions and fluid are only along the axis direction. In contrast, other compartments are fully connected. For example, the glial cells are connected by connexins and form a syncytium, allowing the intra-compartment fluxes flow in both axial and radial directions.

• Communications between compartments: The communications among different compartments are illustrated in Fig. 3. Especially, there is no direct interaction between glial (or perivascular space) and axon compartments. Interactions occur only through changes in concentration, electrical potential, and flows in ECS [28].

The details of the mathematical model can be found in the SI.

3. Results and Discussion

Our coupled ion and fluid transport model can be used for a wide range of studies. In this paper, we focus on the issue of potassium clearance in the optic nerve, leaving out many interesting questions to be explored in follow-up papers. In this section and the rest of our paper, we present simulation results and some discussions with the aim of understanding how glial cells and perivascular spaces facilitate potassium clearance during and after a train of stimulus.

As in Ref. [29], The model is solved using the Finite Volume Method on a uniform mesh with axial symmetry, with equal discretization in the radial and axial directions, i.e., $N_r = N_z = N = 20$ and the time step is fixed at $\delta t = 10^{-1}$ in dimensionless units. As a convergence criterion, the simulation is considered to reach steady state when the maximum variation of all variables between two successive time steps falls below 10^{-8}. To further ensure numerical stability, we adopt conservative flux formulations and implicit time stepping. All variables are monitored to remain within physiologically meaningful ranges throughout the simulation. The code was developed and executed in the Matlab environment. Initially, the resting state of the system is determined through iteration and by setting a fixed volume fraction [30]:

$$\eta^{re}_{ax} = 0.4, \eta^{re}_{gl} = 0.4, \eta^{re}_{ex} = 0.1, \eta^{re}_{pa} = 0.024, \eta^{re}_{pv} = 0.0639, \eta^{re}_{pc} = 0.0121.$$

All values of parameters are listed in **Supplementary Table 1**. Then, these resting-state values are used as initial conditions for the stimulus state.

3.1 Micro-Circulation in the Resting State

Under a pressure gradient of 0.0083 mmHg/mm, CSF flows into the subarachnoid space (SAS) from the intracranial region, with an average velocity of approximately 250 μm/s in the z-direction, consistent with previous findings [31]. CSF then leaks into perivascular space A. The flow direction in perivascular space A (or V) matches the blood flow in the central retinal artery (or vein). The fluid flow in perivascular space C adjusts dynamically through exchanges with other compartments, primarily influenced by perivascular space V due to a larger pressure gradient at boundary Γ_1, with fluid exiting the optic nerve at boundary Γ_2 under membrane boundary conditions.

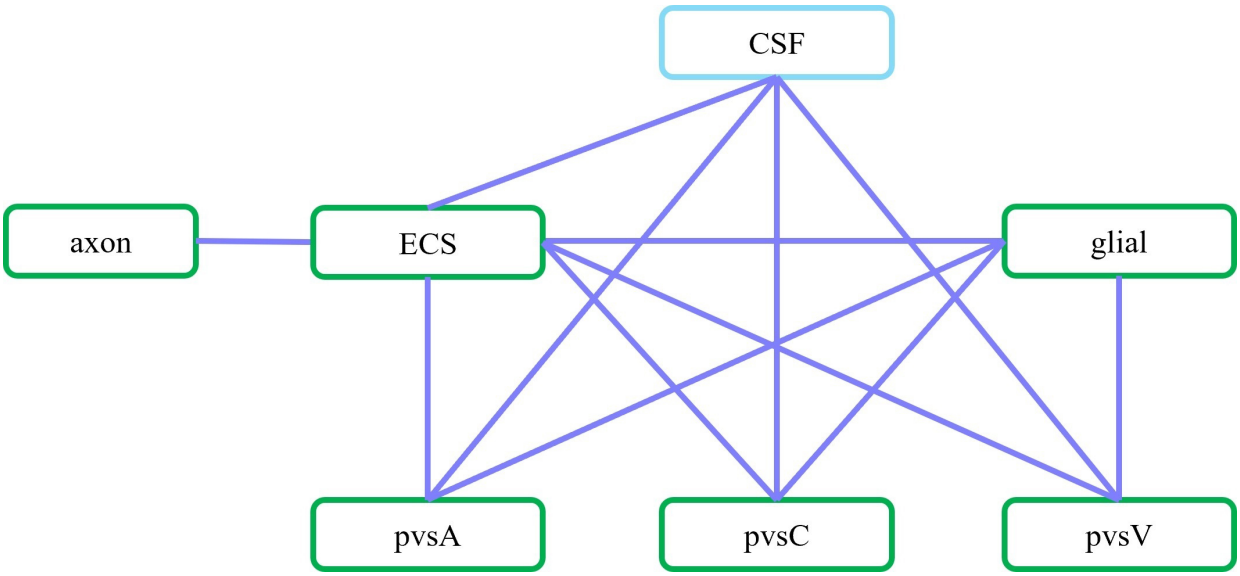

Fig. 3. Schematic of communication between different compartments. In the optic nerve Ω_{OP} region, the ECS exchanges fluid and ions with the axon, glial, the pvsA, the pvsV and the pvsC; glial exchanges fluid and ion with the ECS, the pvsA, the pvsV and the pvsC; CSF exchanges fluid and ions with the ECS, the pvsA, the pvsV, and the pvsC by across the pia mater in Γ_7, see Fig. 2. This figure was drawn using MATLAB (R2023b, MathWorks, Inc., Natick, MA, USA). ECS, extracellular space; CSF, cerebrospinal fluid; pvs, perivascular spaces.

In perivascular space A, the spatially averaged fluid velocity under a 0.007 mmHg/mm pressure gradient in the z-direction is 5 µm/s from the intracanalicular space to the intraorbital region. In perivascular space V, the spatially averaged fluid velocity in the z-direction under a –0.012 mmHg/mm pressure gradient is 4 µm/s from the intraorbital region to the intracanalicular space. These results align with the observations in [17,32].

Simultaneously, fluid flows from pvsA into the ECS and the glial compartment through gaps and Aquaporin channels located near or on the glial cell feet [14], and then into perivascular space V. Fluid also moves from the ECS into the glial compartment, in agreement with the glymphatic system's role [5,13,33].

3.2 Micro-Circulation in the Stimulated State

This section examines the glymphatic system's role (including glial cells and perivascular spaces) in metabolic waste clearance during stimulation. As depicted in Fig. 4, the stimulus is applied to the axon membrane within the region $R_a < r < r_{sti} < R_b$ at a specified location $z = z_0$, with $\theta \in [0,\ 2\pi]$. We differentiate between the stimulated and non-stimulated regions in the optic nerve Ω_{OP}, where electrical signals propagate in the z-direction within the axon compartment. The stimulus frequency is 50 Hz (T = 0.02 s) with a duration of 0.2 s. Each stimulus has a current strength of $I_{sti} = 3 \times 10^{-3}$ A/m^2 and lasts for 3 ms.

3.2.1 Ionic Circulation and Potassium Clearance

This section explores ionic circulation between stimulated and non-stimulated regions. During stimulation, as shown in Fig. 5a, Na^+ ions enter the axon while K^+ ions leak from the axon into the ECS (see Fig. 5i), leading to potassium accumulation in the stimulated region. Snapshots of potassium concentration in the ECS, shown in Fig. 6, indicate that potassium concentration initially rises in the stimulated region, reaching up to 5.3 mM. Subsequently, through the buffering function of the glymphatic system, the accumulated potassium is transported from the stimulated to the non-stimulated region, lowering the overall concentration in the optic nerve to 4.9 mM.

Fig. 7a illustrates three mechanisms for buffering the accumulated potassium: the glial compartment, the perivascular space, and diffusion within the ECS. Fig. 7b illustrates the potassium spatial buffering and water circulation between ECS and glial compartment. The interaction between osmotic pressure difference, convection, diffusion, and electrical drift is demonstrated in detail.

• Glial Compartment: The glial compartment is the primary pathway for potassium buffering, protecting axons. Potassium accumulation in the stimulated region generates a Nernst potential $E^K_{gl,ex}$, across the glial membrane, driving potassium flow from the extracellular space into the glial compartment, as shown in Fig. 5b. This rapid influx raises the local electric potential, facilitating potassium redistribution from the stimulated to the non-stimulated region. Due to connexins, the glial compartment behaves as an electrical syncytium, causing the membrane potential in the non-stimulated region to also become more positive. However, the glial potassium Nernst potential in the non-stimulated region remains near its resting state, resulting in an outward potassium flux from the glial compartment.

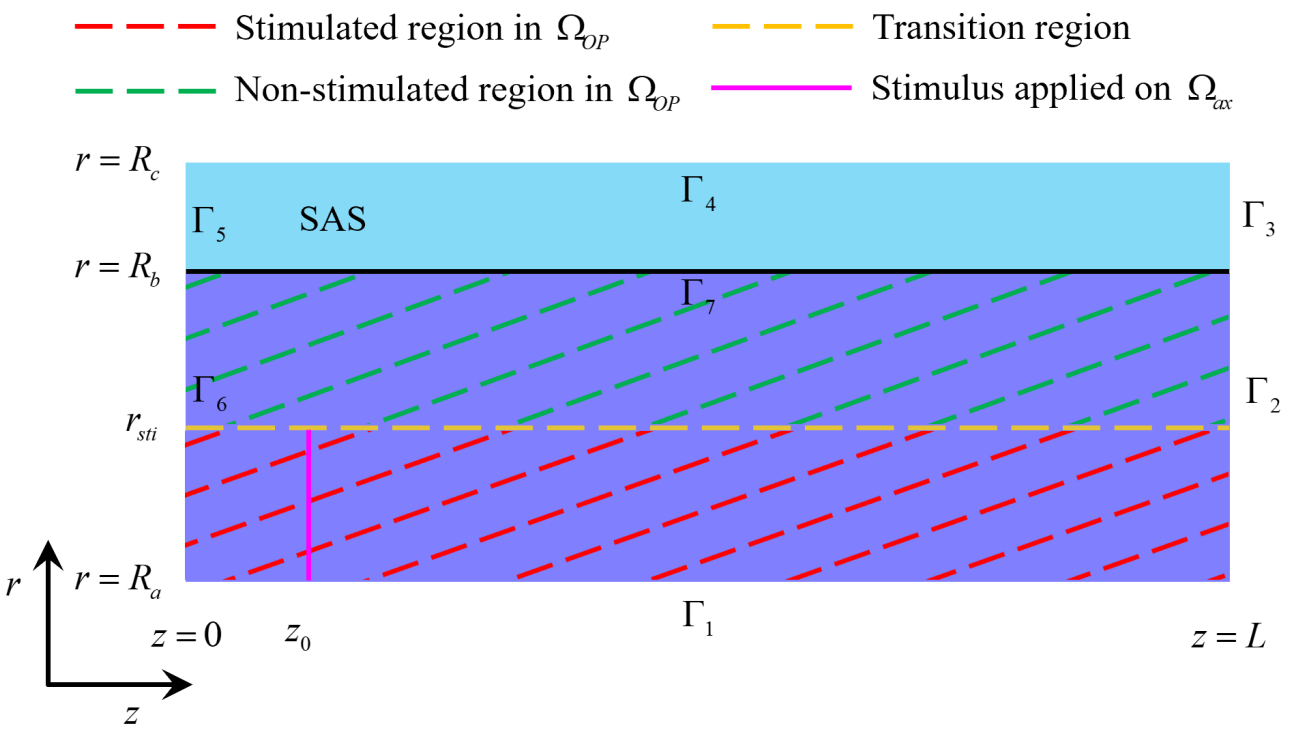

Fig. 4. Stimulated and non-stimulated regions in the optic nerve (Ω_{OP}). The stimulus is applied to the axon membrane within the region $R_a < r < r_{sti}$ at a specified location $z = z_0$. This figure was drawn using MATLAB (R2023b, MathWorks, Inc., Natick, MA, USA).

Fig. 8a shows that during the stimulus, electric drift flux primarily buffers potassium, while post-stimulus, convection flux driven by water circulation becomes dominant.

• Perivascular Space: The perivascular space serves as a secondary pathway for potassium buffering. Potassium leaks from the ECS into the perivascular space through gaps between astrocytes' endfeet (see Fig. 5f–h), and some potassium from the glial compartment also enters via channels on astrocytes' endfeet (see Fig. 5c–e). Potassium is transported from the stimulated region to the non-stimulated region through convection and diffusion. In the non-stimulated region, potassium leaks back from the perivascular space into the ECS. Fig. 8c–e shows that diffusion flux plays a key role in potassium buffering in the perivascular spaces. Convective flow driven by pressure differences transports potassium from the SAS to the inner optic nerve. Since potassium concentrations in perivascular spaces A, V, and C are much lower than in the glial compartment, the contribution of electric drift to potassium buffering is negligible. During stimulation, perivascular spaces A, V, and C serve as additional pathways for potassium transport from the stimulus region to the non-stimulus region. After stimulation, perivascular spaces V and C continue buffering potassium, while in perivascular space A, convection flux suppresses diffusion, leading to potassium flux directed from the pia mater to the optic nerve center.

• Diffusion in the ECS: As shown in Fig. 8b, the connectivity of the ECS facilitates direct diffusion of accumulated potassium from the stimulated to the non-stimulated region. Fig. 9h illustrates that the total accumulated K^+ buffering through ECS via diffusion is comparable with the glial compartment.

A detailed illustration of potassium microcirculation between the different compartments is available in **Supplementary material Fig. 1**. And the sodium flux inside each domain can be found in **Supplementary material Fig. 3**.

Fig. 9 presents the cumulative potassium flux (total potassium flux integrated over time). The results indicate that the cumulative potassium flux through the glial membrane is twice as large as the radial cumulative potassium flux inside the ECS, two orders of magnitude larger than in pvsC, and three orders of magnitude larger than in pvsA and pvsV within the stimulated ECS. Concurrently, the cumulative potassium flux through the glial membrane into pvsV is 1.5 times the radial cumulative potassium flux inside the glial membrane and an order of magnitude larger than in pvsA and pvsC within the stimulated glial compartment during a train of stimuli.

In summary, these numerical results confirm that the glial compartment is the most critical and rapid pathway for potassium transport, while the perivascular spaces provide secondary pathways for potassium removal from the stimulated region when neurons fire or stop firing. Over time, potassium circulation and concentrations in each compartment return to the resting state.

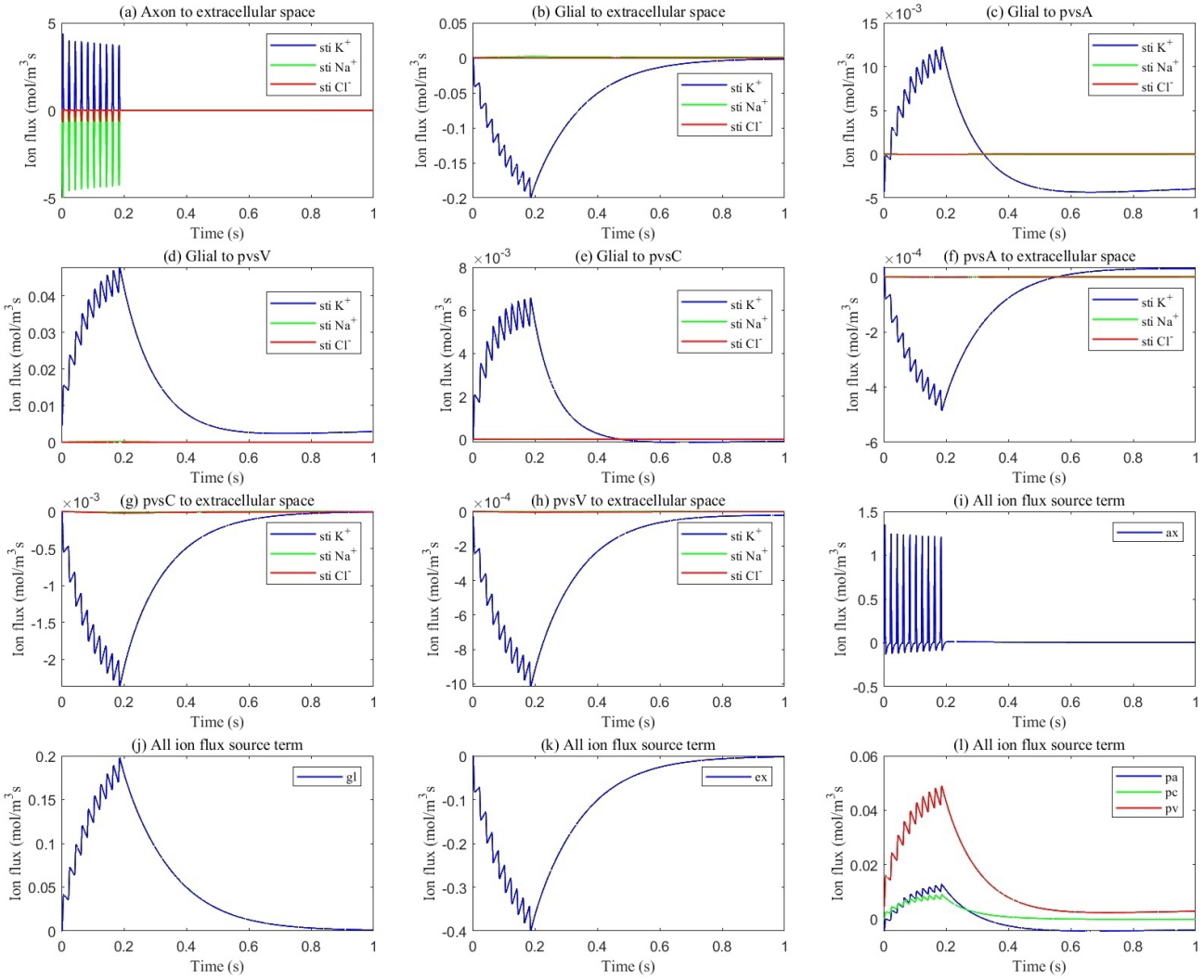

Fig. 5. Average transmembrane ion flux in the stimulated region. (a) from axon to ECS; (b) from glia to ECS; (c) from glia to pvsA; (d) from glia to pvsV; (e) from glia to pvsC; (f) from pvsA to ECS; (g) from pvsC to ECS; (h) from pvsV to ECS; (i) total ion flux flows into axon; (j) total ion flux flows into glia; (k) total ion flux flows into ECS; (l) total ion flux flows into pvs.

3.2.2 Fluid Circulation

While this paper primarily focuses on potassium clearance, we provide a brief summary of fluid circulation in **Supplementary material Fig. 2**, with further details to be explored in a separate paper. Fluid circulation during and after stimulation is driven by two primary forces: hydrostatic pressure differences and osmotic pressure differences. See Fig. 5i–l, the selective permeability of the cell membrane to different ions leads to variations in osmotic pressure between different components. Hydrostatic pressure gradients within the subarachnoid space (SAS) and perivascular spaces direct the movement of CSF and interstitial fluid through the optic nerve compartments. Simultaneously, osmotic pressure, influenced by ionic microcirculation, drives fluid exchange between the ECS, glial compartments, and perivascular spaces. These mechanisms work together to facilitate fluid redistribution, ensuring efficient clearance of metabolic waste and maintaining homeostasis between the stimulated and non-stimulated regions. The dynamic interaction between these forces allows fluid circulation to adapt in response to neuronal activity, supporting the glymphatic system's overall function in the optic nerve.

3.3 Effects of Glial Compartments on Potassium Clearance

In this section, we investigate the role of the glial compartment in extracellular potassium buffering by varying the transmembrane ionic conductance (g^i_{gl}), hydraulic permeability, and modifying connexin connectivity, which reduces diffusion coefficients and permeability within the glial compartment.

3.3.1 Membrane Ionic Conductivity

Research suggests that in neurodegenerative diseases, oxidative stress and inflammation can impair ion channels on astrocytes, reducing their conductivity [34,35]. To simulate these effects, we reduced the membrane conductiv-

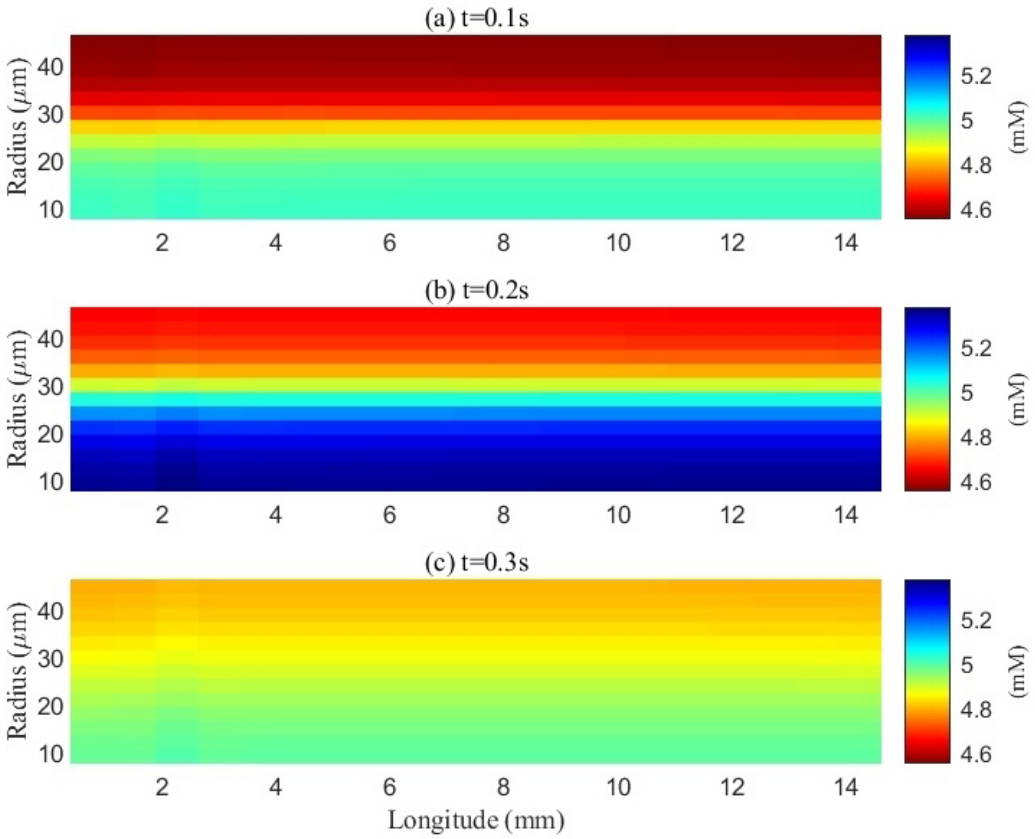

Fig. 6. Spatial distribution of potassium concentration in the extracellular space (ECS) during and after a train of stimuli. a, b, and c represent the spatial distribution of potassium ions at different time points: 0.1 s, 0.2 s, and 0.3 s, respectively. The initial potassium concentration in the ECS was 4.5 mM. Upon electrical stimulation of the axons, action potentials were generated, resulting in potassium efflux into the ECS and a localized increase in potassium concentration within the stimulated (lower) region. The potassium concentration in this area peaked at 5.3 mM by the end of the stimulation period (0.2 s). During stimulation, excess potassium also diffused from the stimulated region into adjacent non-stimulated regions. After the cessation of stimulation, the potassium concentration gradually re-equilibrated throughout the ECS.

ity to $\frac{1}{20}$, $\frac{1}{30}$, $\frac{1}{50}$ of the original values. Fig. 10 shows the spatial distribution of extracellular potassium at various time points for different membrane conductance levels. As previously discussed, potassium clearance occurs via three main pathways: diffusion in the ECS, buffering by the glial compartment, and transport through the perivascular spaces.

As glial membrane conductance decreases, the transmembrane flux through the glial compartment is reduced (see Fig. 11c–f), resulting in less efficient potassium clearance from the ECS (see Fig. 11a). When the conductance is reduced to $\frac{1}{20}$ of its original value, the perivascular spaces compensate by increasing their transmembrane flux, becoming the primary mechanism for potassium clearance (see Fig. 11g–i). This reduces the rate of potassium accumulation in the non-stimulated region (see Fig. 11b). However, the difference in potassium concentration between the stimulated and non-stimulated regions increases, leading to enhanced diffusion in the ECS (see Fig. 12).

The role of the glial compartment is not limited to potassium buffering. Fig. 13 shows the results during the first stimulus. We applied the same stimulation protocol. The stimulus region showed minimal variation in axonal membrane potential. See Fig. 13c. At the onset of stimulation, the field potential in the extracellular region decreases (see Fig. 13a) as Na^+ channels activate, allowing more Na^+ to enter the axon. This raises the axonal potential and causes potassium to leak out of the glial compartment because the transmembrane potential ($\phi_{gl} - \phi_{ex}$) is higher than the Nernst potential ($E^K_{gl,ex}$) (see Fig. 13d). This process prevents the extracellular potential from dropping too low.

During the later stages of the action potential, K^+ channels are activated, and more K^+ ions enter the ECS, making the Nernst potential $E^K_{gl,ex}$ more positive and driving K^+ into the glial compartment (see Fig. 13d). However, if the conductance drops too low (below $\frac{1}{30}$ of the original value), less potassium flows from the glial compartment to ECS (see Fig. 13d), resulting in a more negative extracellular potential. Due to the rapid propagation of the electric potential, the non-stimulated region also experiences a drop in extracellular potential (see Fig. 13b), which causes

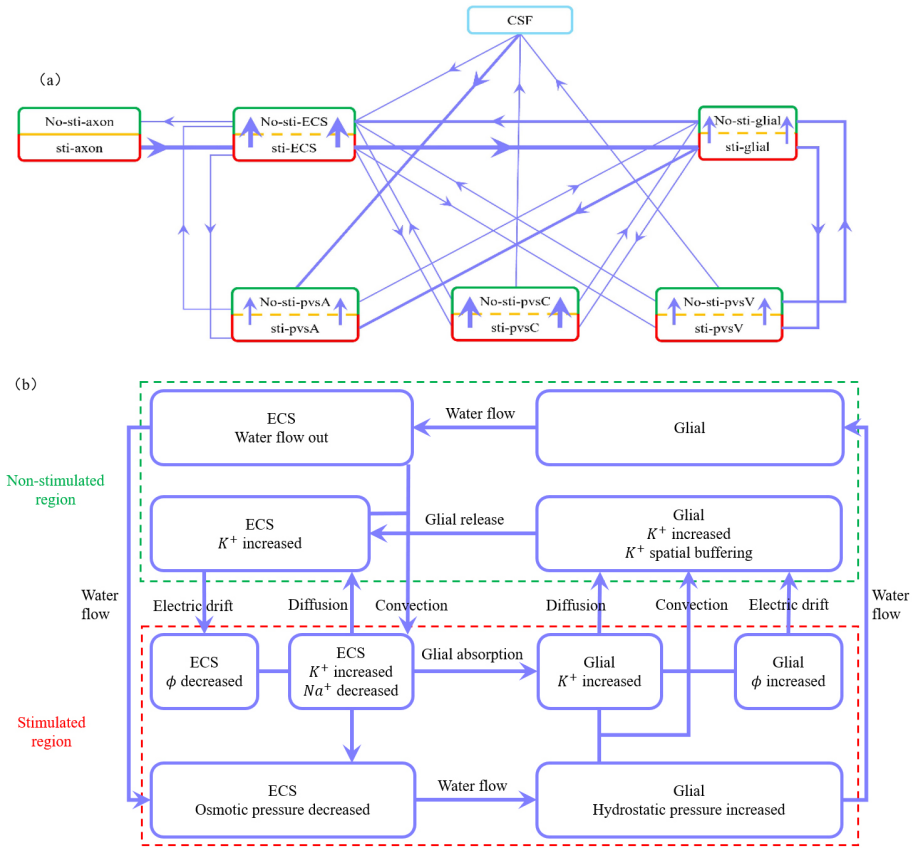

Fig. 7. Illustration of microcirculation and the roles of diffusion, convection and electric drift. (a) Schematic of potassium flux between the stimulated (lower) and non-stimulated (upper) regions, as well as transmembrane flux between different compartments during stimulation. Red boxes represent stimulated regions, and green boxes represent non-stimulated regions. The thickest lines indicate fluxes around 10^{-1} mol/(m^3s), moderately thick lines represent fluxes around 10^{-2} mol/(m^3s), and the thinnest lines indicate fluxes less than 10^{-3} mol/(m^3s). (b) Schematic description for potassium spatial buffering and water circulation between ECS and glial compartment. When axon is stimulated to release an action potential, potassium ions flow out while sodium ions flow in, leading to an increase potassium concentration and a decrease in osmotic pressure in ECS. In the stimulated region, potassium ions enter glial from the ECS through the glial membrane, raising the electrical potential in the glial compartment. The water flow out of ECS into glial with the osmotic pressure different. Within the glial compartment, the hydrostatic pressure and the potassium concentration are increased in stimulated region. The water flow from the stimulated region into the non-stimulated region. And the potassium diffusion, convection, electric drift are all causing potassium to flow from the stimulated region to the non-stimulated region. But the electric drift dominates. In the non-stimulated region, potassium leak back into the ECS by flowing out of the glial through the glial membrane. And due to the osmotic pressure difference, water flows from the glial compartment back into the ECS. Within the ECS, potassium carried by water convection and electric drift from the non-stimulated region back to the stimulated region, while diffusion dominates, causing potassium to flow from the stimulated region to the non-stimulated region. the hydrostatic pressure difference drives water to flow back from the non-stimulated region to the stimulated region, completing the cycle. This figure was drawn using MATLAB (R2023b, MathWorks, Inc., Natick, MA, USA).

the axon membrane potential to increase. This leads to the activation of Na^+ channels in the non-stimulated region, generating an action potential (see Fig. 14c,d) and releasing more potassium into the ECS, creating a feedback loop that exacerbates potassium accumulation. However, neither the Baseline nor the 1/20 condition produced this abnormal discharge pattern. See in Fig. 14a,b. In this case, the concentration difference between the stimulated and non-stimulated regions is smaller, and the diffusion flux in the ECS decreases, as shown in Fig. 12. This is consistent with the clinic's observation that When glial ionic conductance is impaired, it can lead to conditions such as epilepsy, where excessive and synchronized neuronal activity occurs [36].

In summary, glial cell ionic conductivity, particularly involving potassium regulation, is crucial for preventing neuronal hyperexcitability and the development of epilepsy. Dysfunction in these mechanisms can lead to disrupted ionic homeostasis, contributing to the occurrence of seizures.

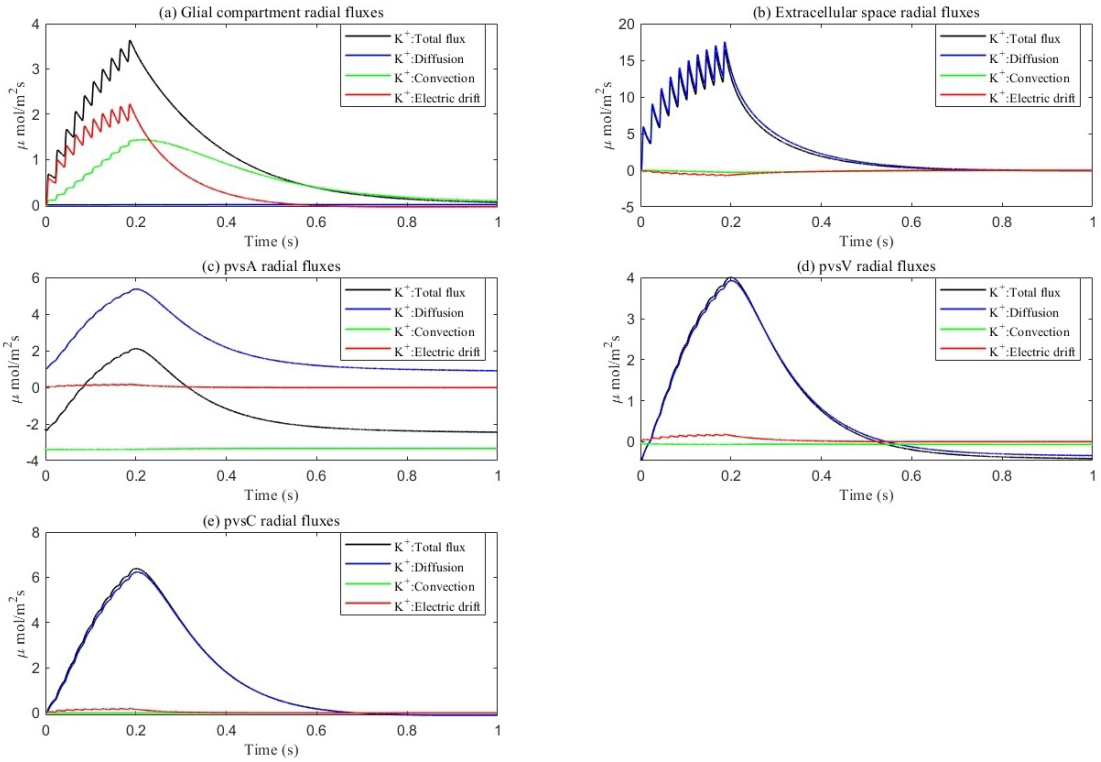

Fig. 8. Average radial direction potassium flux components within each compartment. (a–e) represent different components, respectively. (a) glial compartment. (b) ECS. (c) pvsA. (d) pvsV. (e) pvsC. Total flux equals diffusion flux plus convection flux plus electric drift flux. In glial compartment, the electric drift is dominant. In ECS and PVS, the diffusion is dominant.

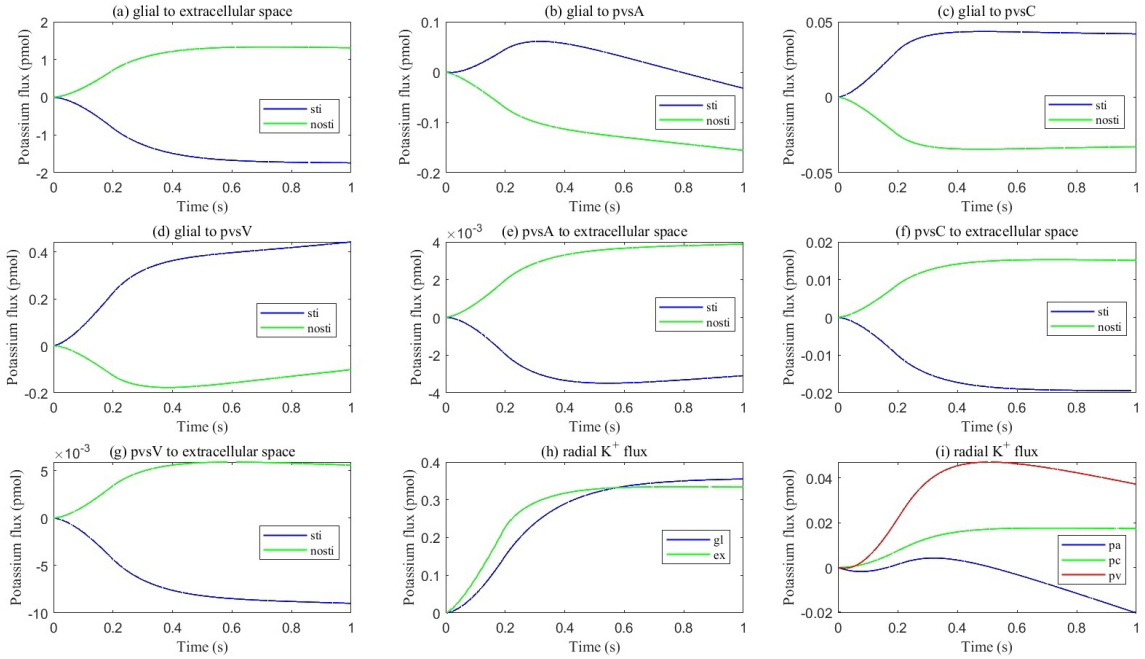

Fig. 9. Cumulative transmembrane flux between different comparts. (a–g) Cumulative transmembrane potassium fluxes in the stimulated and non-stimulated regions after neuronal firing stops. (h,i) Radial cumulative potassium fluxes within compartments after neuronal firing stops.

3.3.2 Connexin Connectivity

Connexins in glial cells, particularly astrocytes, form gap junctions that facilitate direct communication between cells by allowing the passage of ions, small molecules, and signaling substances. These connexins play a crucial role in maintaining ionic balance, including potassium clearance

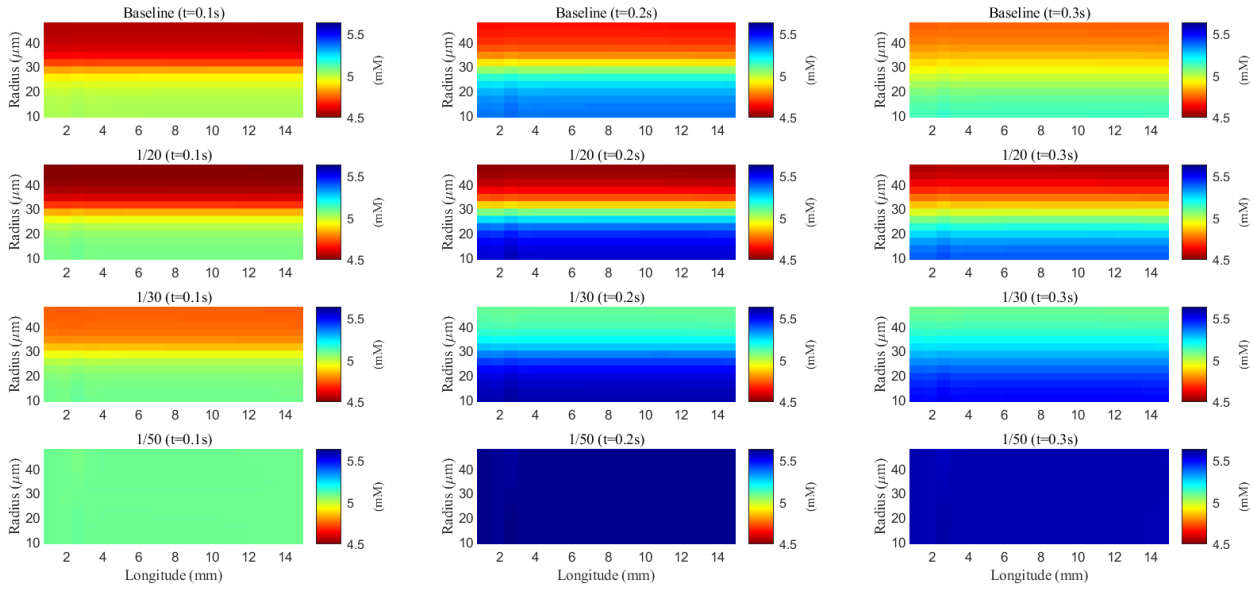

Fig. 10. Spatial distribution of potassium concentration during and after a train of stimuli in the ECS. Different rows are results with different membrane conductance; Different columns are results at different time slots.

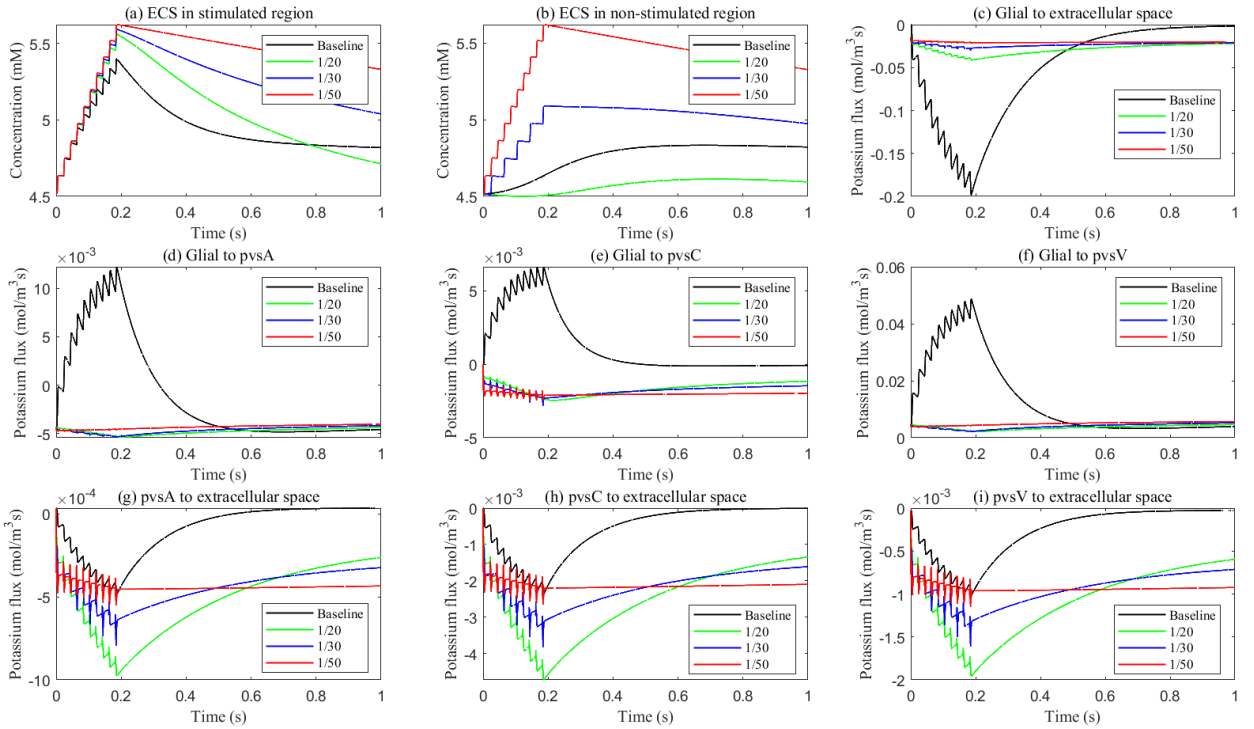

Fig. 11. Potassium concentration and transmembrane potassium flux with different glial membrane conductance. (a,b) The potassium concentration in the stimulated and non-stimulated regions. (c–i) The transmembrane potassium flux in stimulated region.

in the brain's ECS. However, in certain pathological conditions or through experimental interventions, connexin function can be disrupted or blocked [37]. Such dysfunction reduces the connectivity of the glial compartment. In our simulation, we decrease the diffusion coefficients D^i_{gl} and permeability κ_{gl} by factors of 10^{-1}, 10^{-2}, and 10^{-4} to examine the effects of impaired connexin connectivity.

After a stimulus, potassium, and fluid flow from the extracellular space into the glial compartment due to differences in Nernst potential and osmotic pressure. Fig. 15 shows the spatial distribution of electric potential within the glial compartment (long-term behavior can be found in **Supplementary material Fig. 4**). As connexin connectivity decreases, the intracellular conductance $\sum_i z_i^2 e D_{gl}$ also

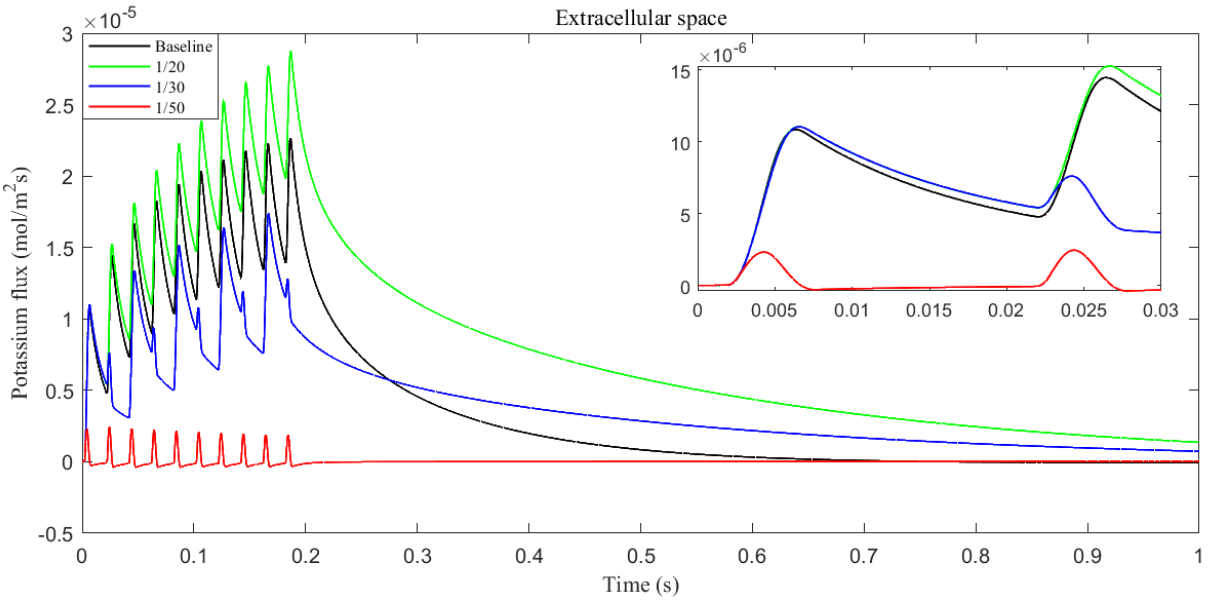

Fig. 12. Average radial potassium flux within the ECS with different glial membrane conductance. The subplot shows the radial potassium flux during a single action potential.

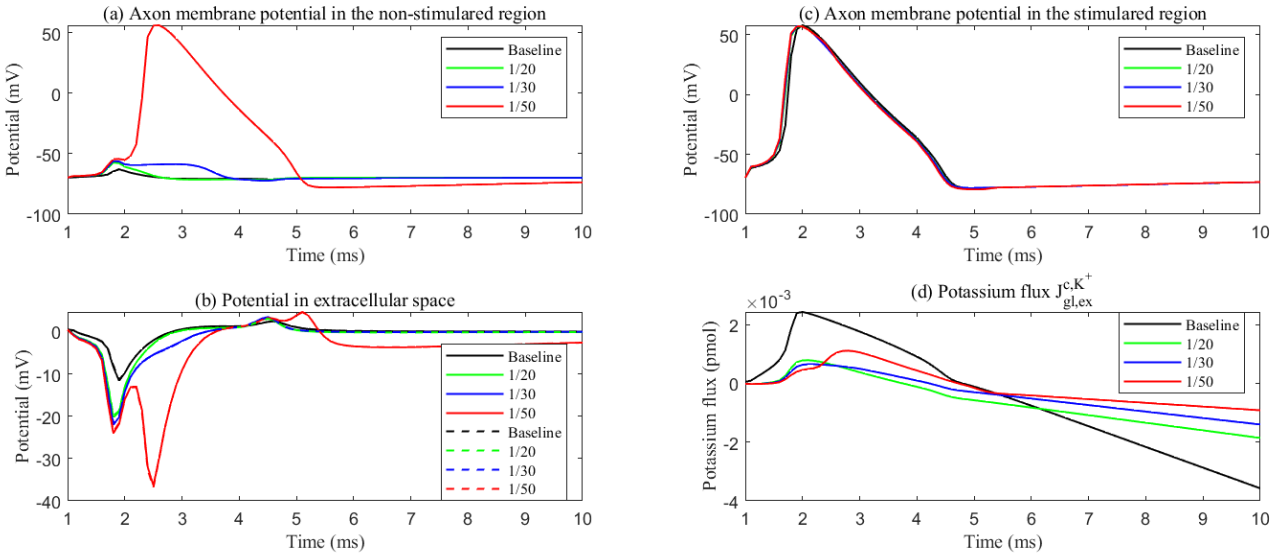

Fig. 13. Membrane potential with different membrane conductance. (a) Axon membrane potential in the non-stimulated region. (b) The electric potential in the ECS in the stimulated region (solid line) and non-stimulated region (dash line). (c) Axon membrane potential in the stimulated region. (d) The cumulative potassium flux through the passive ion channel on the glial membrane from the glial compartment to the ECS. Different lines mean different glial membrane conductance. During sustained stimulation, potassium flux from glial to the ECS maintains ECS potential within physiological range, thereby preventing passive action potential generation in non-stimulated regions.

decreases, which inhibits the propagation of the electric potential from the stimulated region to the non-stimulated region. As a result, the membrane potential in the glial compartment of the stimulated region becomes more elevated compared to the baseline.

Although potassium concentration remains nearly constant (see Fig. 16), due to the swelling of the glial compartment, the rising glial membrane potential (see Fig. 16b) reduces the transmembrane potassium influx, as shown in Fig. 17f. The reduction in permeability and diffusion within the glial compartment leads to a significant decrease in the potassium buffering flux (see Fig. 17a). In this scenario, the glial compartment in the stimulated region acts as a reservoir, absorbing excess potassium and protecting the axonal cells.

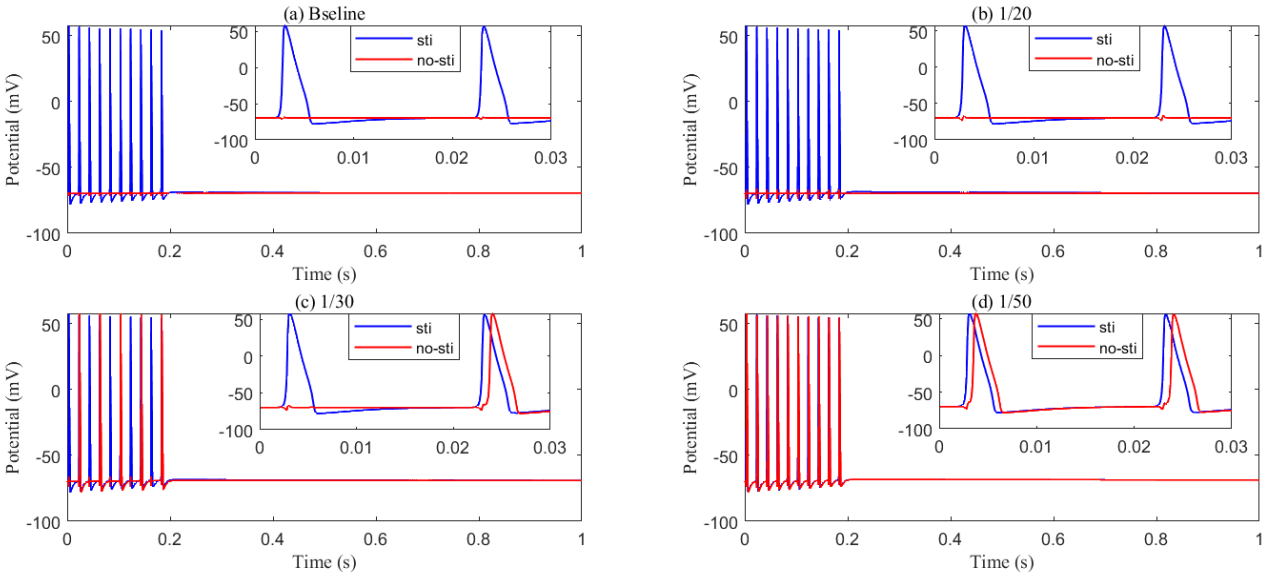

Fig. 14. Recording axon membrane potential in the stimulated (blue) and non-stimulated (red) region with different glial membrane conductance. (a) Baseline results; (b) conductance reduced to be 1/20 of baseline; (c) conductance reduced to be 1/30 of baseline; (d) conductance reduced to be 1/50 of baseline. As the membrane conductance of glial cells decreases, abnormal axonal firing occurs, generating passive action potentials in non-stimulated regions.

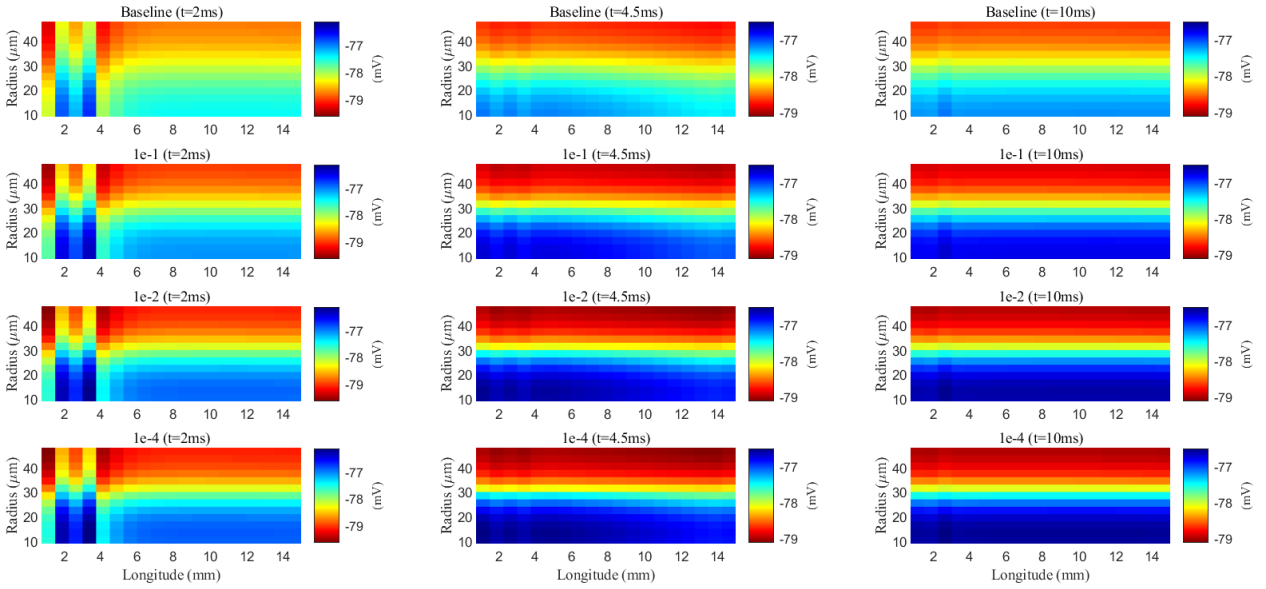

Fig. 15. Spatial distribution of membrane potential during a stimulus in the glial compartment. Different rows are results with different connectivity of glial compartments. Different columns are results at different time slots.

At the same time, the elevated electric potential in the glial compartment enhances the flux from the glial compartment to the perivascular spaces (see Fig. 18a–c), increasing the intra-compartment flux within the perivascular space (see Fig. 17c–e). The reduced permeability within glial compartment enhances the flow of potassium ions from the ECS to the pvs (see in Fig. 18d–f), while the radial potassium flux in the extracellular space exhibits a slight but insignificant increase (see in Fig. 17b). This suggests that the perivascular spaces take on a more prominent role in buffering potassium in these conditions (see Figs. 5,6 in **Supplementary material**). However, compared to the glial electric drift mechanism, convection-based transport in the perivascular spaces is less efficient for potassium clearance (see Fig. 16d).

In summary, the glial pathway is the most important mechanism for potassium buffering and clearance, while the perivascular space pathway serves as the second most important. When the pathways of glial compartment are compromised, whether it is the glial membrane or the in-

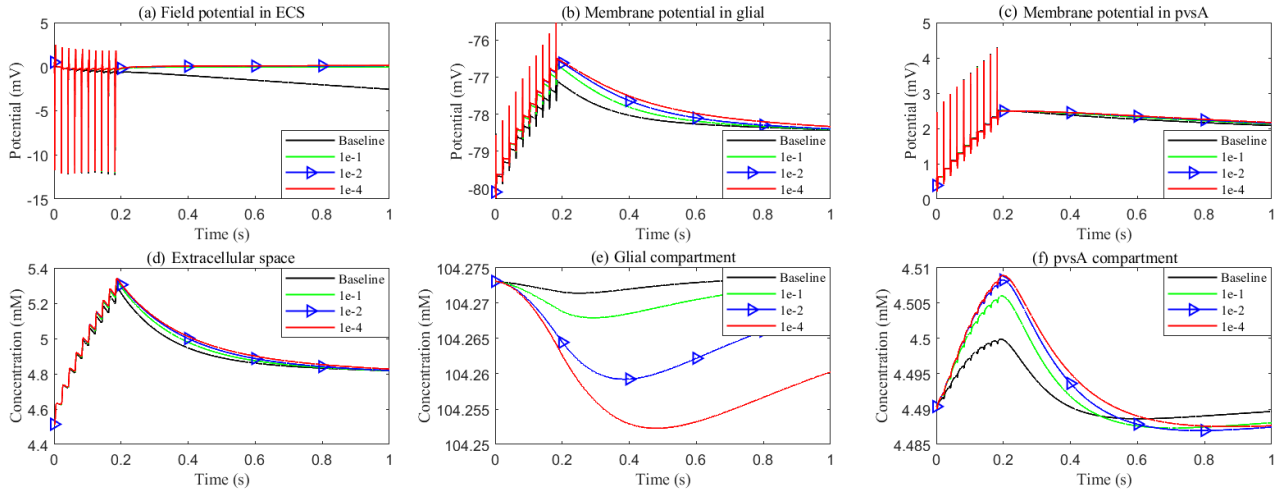

Fig. 16. Effects of glial connexin connectivity on the membrane potential and potassium clearance. (a–c) Field potential and membrane potential in the stimulated region. (d–f) Potassium concentration in the stimulated region.

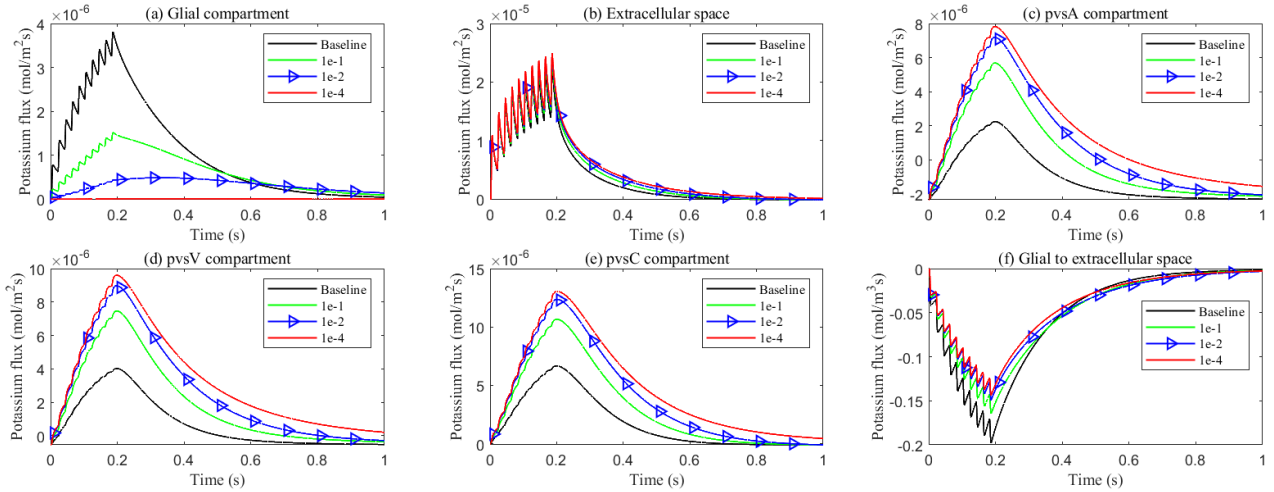

Fig. 17. Effects of glial connexin connectivity on the transmembrane potassium flux. (a–e) Average radial potassium flux in the intradomain with varying levels of glial connexin connectivity. (f) Average transmembrane potassium flux from glial to ECS in the stimulated region.

ternal pathways of the glial compartment, the perivascular space pathway takes on a more significant role in buffering potassium ions from the ECS.

4. Conclusions

This study presents a multicompartment model of the optic nerve that integrates ionic electrodiffusion, osmotic water transport, and convective fluid flow across axons, glial cells, the ECS, and perivascular domains. By extending earlier frameworks, we incorporate glial–vascular interactions to investigate potassium buffering and clearance following neuronal stimulation.

Our simulations demonstrate that potassium released from axons during activation accumulates in the ECS and is rapidly cleared through two major pathways: (i) uptake by glial cells, and (ii) fluid-mediated redistribution via perivascular spaces. The efficiency of this clearance strongly depends on glial membrane conductance and intercellular connexin permeability. Reduced glial conductance leads to ectopic neuronal excitation, resembling epileptic activity, while impaired gap junction connectivity increases reliance on perivascular drainage. These results highlight the cooperative role of glia and vasculature in maintaining extracellular ionic homeostasis. The model reveals that potassium transport is primarily driven by electric drift within glial syncytia, while osmotic and convective forces regulate fluid movement. This interaction enables volume preservation and ion redistribution under varying physiological conditions.

While our model provides valuable insights, it has several limitations that could be addressed in future studies:

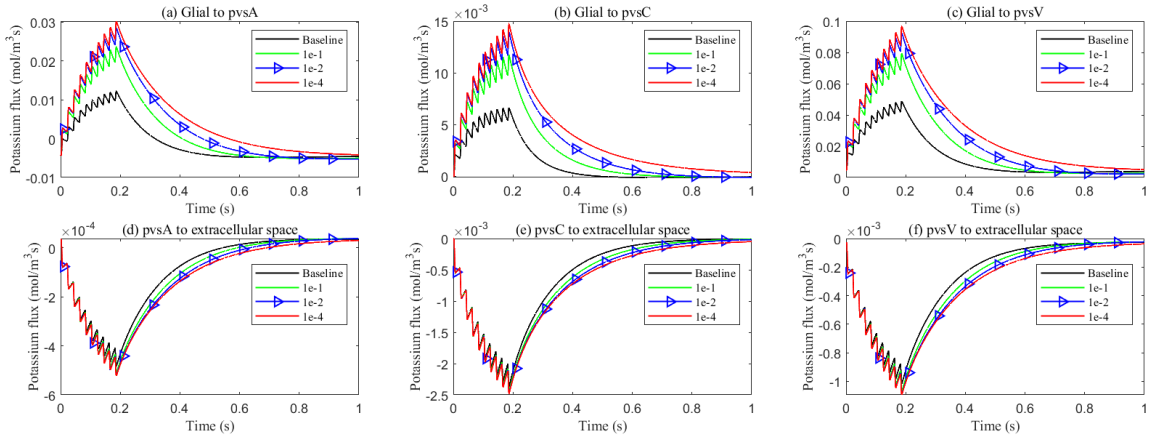

Fig. 18. Average transmembrane potassium flux on perivascular spaces with varying levels of glial connexin cnnectivity in the stimulated region. Transmembrane K^+ fluxes (a) from glia to pvsA; (b) from glia to pvsC; (c) from glia to pvsV; (d) from pvsA to ECS; (e) from pvsC to ECS; (f) from pvsV to ECS.

• Simplified Representation of K^+ Channels: In the current model, potassium transport mechanisms are categorized into passive and active components. All passive fluxes—arising from various K^+ channels and cotransporters—are aggregated into an effective macroscale membrane conductance, capturing their collective influence without resolving each individual mechanism. Active transport via the Na^+/K^+-ATPase pump is explicitly modeled, as it plays a critical role in maintaining ionic gradients and resting potential. This simplified representation balances biophysical realism and computational tractability. However, we acknowledge that distinct potassium channels (e.g., voltage-gated, inwardly rectifying, calcium-activated) exhibit different gating kinetics and spatial distributions, which may influence local dynamics, particularly under pathological conditions. As more quantitative data on channel kinetics and densities become available, the model can be extended to incorporate these components explicitly. The current framework is designed to be modular and flexible, enabling such enhancements without substantial increases in computational complexity.

• Homogenization of Perivascular Spaces and Glial Compartment: In this model, we adopt a coarse-grained representation of perivascular and glial compartments, which simplifies anatomical geometry by averaging structural features over space. While we do not resolve fine-scale anatomical heterogeneity—such as local variations in vascular branching or glial cell morphology—the model allows spatial variation in volume fractions due to dynamic fluid exchange, enabling it to capture physiologically relevant redistribution under different conditions. This formulation strikes a balance between biophysical realism and computational tractability. In future work, we aim to incorporate more detailed anatomical variability by introducing spatially varying transport parameters or integrating imaging-derived structural data.

Despite these limitations, our model is inherently designed to describe multidomain coupling in central nervous system (CNS) microcirculation, where ionic electrodiffusion, fluid flow, and cellular compartmentalization are tightly integrated. It is particularly well-suited for structures with approximately cylindrical geometry, such as the optic nerve. However, when applying this model to other neural structures with significantly different geometries—such as the retina, which has a hemispherical shape—modifications would be necessary. For instance, the assumption of axial symmetry may no longer hold, and the geometry would need to be reparametrized accordingly. One approach is to introduce a deformation or curvature parameter that adjusts the radial coordinate as a function of axial distance, allowing the model to approximate a curved domain while preserving numerical efficiency. In addition, cell types and their layout also need to be taken into consideration.

In addition, different tissue types may involve distinct membrane surface areas, permeability profiles, and ion channel distributions. These physiological differences can be incorporated into the current framework by adjusting the relevant coefficients and source terms, without altering the underlying mathematical structure. Although the model does not explicitly resolve fine-scale anatomical heterogeneity, it captures emergent spatial variation in compartmental volume fractions driven by fluid transport. This coarse-grained approach offers a practical and physiologically meaningful basis for system-level investigations. In future work, we plan to refine the model by incorporating spatially varying parameters—such as ion pump density and vascular architecture—or by integrating image-derived geometries to simulate region-specific dynamics under both healthy and pathological conditions.

Moreover, this model holds significant potential for simulating pathological conditions such as epilepsy, in which disrupted ion homeostasis, impaired fluid dynam-

ics, and compromised clearance mechanisms contribute to disease progression. The insights gained from our simulations—such as abnormal potassium accumulation and ectopic axonal excitation in response to altered glial ion permeability—can help identify key physiological thresholds and failure points. These findings may inform the development of therapeutic strategies aimed at modulating glial function or enhancing solute clearance via perivascular pathways, ultimately supporting neuronal stability and resilience.

Abbreviations

C_l^i, Ion i concentration in compartment l; k_e^l, Electroosmotic in compartment l; ϕ_l, Electric potential in compartment l; $\mathrm{M}_{\_(a,b)}$, Interface area form a to b in per unit control volume; p_l, Electric potential in compartment l; κ_l, Fluid permeability in compartment l; η_l, Volume fraction in compartment l; μ, Fluid viscosity; O_l, Osmotic concentration in compartment l; $L_{a,b}$, Hydrostatic permeability of interface form *a* to *b*; u_l, Fluid velocity inside of compartment l; $g_{a,b}^i$, Conductance of interface form compartment *a* to *b* for ion i; ${\mathrm{j}_l}^i$, Electric potential in compartment l; $\bar{g}^i$, Maximum conductance of axon membrane for ion i; $U_{a,b}$, Fluid flux across the interface form *a* to *b*; g_{leak}^i, Leak conductance of axon membrane for ion i; $J_{a,b}^i$, Ion i flux across the interface form *a* to *b*; K_l, Stiffness constant of the interface for compartment l; $J_{a,b}^{p,i}$, Active ATP based ion i pump form *a* to *b*; τ_l, Tortuosity of compartment l; $J_{a,b}^{c,i}$, Passive source form compartment *a* to *b*; D_l^i, Diffusion coefficient of i ion in compartment l; $I_{a,1}$, Max current of α_1-*Na/K* pump on *a* membrane; T, Temperature; $I_{a,2}$, Max current of α_2-*Na/K* pump on *a* membrane; k_B, Boltzmann constant; A_l, Negative charged protein density in compartment l; e, The magnitude of the electron charge; N_A, Avogadro constant.

Availability of Data and Materials

The datasets used and analyzed during the current study are available from the corresponding author on reasonable request.

Author Contributions

HH, SX and RE conceived and designed the research study. SFX conducted the research. SFX, HH, ZS, and SX contributed to model development. SFX, ZS, and SX implemented the computational programming. SFX, RE, and SX drafted and revised the manuscript. All authors contributed to editorial changes in the manuscript. All authors read and approved the final manuscript. All authors have participated sufficiently in the work and agreed to be accountable for all aspects of the work.

Ethics Approval and Consent to Participate

Not applicable.

Acknowledgment

Not applicable.

Funding

This work was partially supported by the National Natural Science Foundation of China no.12231004 (H. Huang) and 12071190 (S. Xu).

Conflict of Interest

The authors declare no conflict of interest.

Declaration of AI and AI-Assisted Technologies in the Writing Process

During the preparation of this work, the authors used ChatGPT to improve the language and readability. After using this tool/service, the authors reviewed and edited the content as needed and take full responsibility for the content of the published article.

Supplementary Material

Supplementary material associated with this article can be found, in the online version, at https://doi.org/10.31083/FBL39722.

References

[1] Kofuji P, Newman EA. Potassium buffering in the central nervous system. Neuroscience. 2004; 129: 1045–1056. https://doi.org/10.1016/j.neuroscience.2004.06.008.

[2] Walz W. Role of astrocytes in the clearance of excess extracellular potassium. Neurochemistry International. 2000; 36: 291–300. https://doi.org/10.1016/s0197-0186(99)00137-0.

[3] Bellot-Saez A, Kékesi O, Morley JW, Buskila Y. Astrocytic modulation of neuronal excitability through K^+ spatial buffering. Neuroscience and Biobehavioral Reviews. 2017; 77: 87–97. https://doi.org/10.1016/j.neubiorev.2017.03.002.

[4] Iliff JJ, Wang M, Liao Y, Plogg BA, Peng W, Gundersen GA, *et al*. A paravascular pathway facilitates CSF flow through the brain parenchyma and the clearance of interstitial solutes, including amyloid β. Science Translational Medicine. 2012; 4: 147ra111. https://doi.org/10.1126/scitranslmed.3003748.

[5] Jessen NA, Munk ASF, Lundgaard I, Nedergaard M. The Glymphatic System: A Beginner's Guide. Neurochemical Research. 2015; 40: 2583–2599. https://doi.org/10.1007/s11064-015-1581-6.

[6] Thomas JH. Fluid dynamics of cerebrospinal fluid flow in perivascular spaces. Journal of the Royal Society, Interface. 2019; 16: 20190572. https://doi.org/10.1098/rsif.2019.0572.

[7] Schreder HE, Liu J, Kelley DH, Thomas JH, Boster KAS. A hydraulic resistance model for interstitial fluid flow in the brain. Journal of the Royal Society, Interface. 2022; 19: 20210812. https://doi.org/10.1098/rsif.2021.0812.

[8] Ineichen BV, Okar SV, Proulx ST, Engelhardt B, Lassmann H, Reich DS. Perivascular spaces and their role in neuroinflammation. Neuron. 2022; 110: 3566–3581. https://doi.org/10.1016/j.neuron.2022.10.024.

[9] Selkoe DJ, Hardy J. The amyloid hypothesis of Alzheimer's disease at 25 years. EMBO Molecular Medicine. 2016; 8: 595–608. https://doi.org/10.15252/emmm.201606210.

[10] Verheggen ICM, Van Boxtel MPJ, Verhey FRJ, Jansen JFA, Backes WH. Interaction between blood-brain barrier and glymphatic system in solute clearance. Neuroscience and Biobehav-

ioral Reviews. 2018; 90: 26–33. https://doi.org/10.1016/j.neubiorev.2018.03.028.
[11] Deng W, Liu C, Parra C, Sims JR, Faiq MA, Sainulabdeen A, *et al*. Quantitative imaging of the clearance systems in the eye and the brain. Quantitative Imaging in Medicine and Surgery. 2020; 10: 1–14. https://doi.org/10.21037/qims.2019.11.18.
[12] Hayreh SS. Ischemic optic neuropathy. Progress in Retinal and Eye Research. 2009; 28: 34–62. https://doi.org/10.1016/j.preteyeres.2008.11.002.
[13] Mathieu E, Gupta N, Ahari A, Zhou X, Hanna J, Yücel YH. Evidence for Cerebrospinal Fluid Entry Into the Optic Nerve via a Glymphatic Pathway. Investigative Ophthalmology & Visual Science. 2017; 58: 4784–4791. https://doi.org/10.1167/iovs.17-22290.
[14] Nakada T, Kwee IL, Igarashi H, Suzuki Y. Aquaporin-4 Functionality and Virchow-Robin Space Water Dynamics: Physiological Model for Neurovascular Coupling and Glymphatic Flow. International Journal of Molecular Sciences. 2017; 18: 1798. https://doi.org/10.3390/ijms18081798.
[15] Asgari M, de Zélicourt D, Kurtcuoglu V. Glymphatic solute transport does not require bulk flow. Scientific Reports. 2016; 6: 38635. https://doi.org/10.1038/srep38635.
[16] Bilston LE, Fletcher DF, Brodbelt AR, Stoodley MA. Arterial pulsation-driven cerebrospinal fluid flow in the perivascular space: a computational model. Computer Methods in Biomechanics and Biomedical Engineering. 2003; 6: 235–241. https://doi.org/10.1080/10255840310001606116.
[17] Boster KAS, Cai S, Ladrón-de-Guevara A, Sun J, Zheng X, Du T, *et al*. Artificial intelligence velocimetry reveals in vivo flow rates, pressure gradients, and shear stresses in murine perivascular flows. Proceedings of the National Academy of Sciences of the United States of America. 2023; 120: e2217744120. https://doi.org/10.1073/pnas.2217744120.
[18] Chou D, Chen PY. A machine learning method to explore the glymphatic system via poroelastodynamics. Chaos, Solitons & Fractals. 2024; 178: 114334. https://doi.org/10.1016/j.chaos.2023.114334.
[19] Bohr T, Hjorth PG, Holst SC, Hrabětová S, Kiviniemi V, Lilius T, *et al*. The glymphatic system: Current understanding and modeling. iScience. 2022; 25: 104987. https://doi.org/10.1016/j.isci.2022.104987.
[20] Lothman E, Lamanna J, Cordingley G, Rosenthal M, Somjen G. Responses of electrical potential, potassium levels, and oxidative metabolic activity of the cerebral neocortex of cats. Brain Research. 1975; 88: 15–36. https://doi.org/10.1016/0006-8993(75)90943-9.
[21] Bothwell SW, Janigro D, Patabendige A. Cerebrospinal fluid dynamics and intracranial pressure elevation in neurological diseases. Fluids and Barriers of the CNS. 2019; 16: 9. https://doi.org/10.1186/s12987-019-0129-6.
[22] Zhu Y, Xu S, Eisenberg RS, Huang H. A tridomain model for potassium clearance in optic nerve of Necturus. Biophysical Journal. 2021; 120: 3008–3027. https://doi.org/10.1016/j.bpj.2021.06.020.
[23] Daruich A, Matet A, Moulin A, Kowalczuk L, Nicolas M, Sellam A, *et al*. Mechanisms of macular edema: Beyond the surface. Progress in Retinal and Eye Research. 2018; 63: 20–68. https://doi.org/10.1016/j.preteyeres.2017.10.006.
[24] Nicholson C. Diffusion and related transport mechanisms in brain tissue. Reports on Progress in Physics. 2001; 64: 815. https://doi.org/10.1088/0034-4885/64/7/202.
[25] Hayreh SS. The sheath of the optic nerve. Ophthalmologica. Journal International D'ophtalmologie. International Journal of Ophthalmology. Zeitschrift Fur Augenheilkunde. 1984; 189: 54–63. https://doi.org/10.1159/000309386.
[26] Jonas JB, Berenshtein E, Holbach L. Anatomic relationship between lamina cribrosa, intraocular space, and cerebrospinal fluid space. Investigative Ophthalmology & Visual Science. 2003; 44: 5189–5195. https://doi.org/10.1167/iovs.03-0174.
[27] Lai WM, Mow VC. Transport of multi-electrolytes in charged hydrated biological soft tissues. Transport in Porous Media. 1999; 34: 143–157. https://doi.org/10.1023/A:1006561408186.
[28] Sibille J, Dao Duc K, Holcman D, Rouach N. The neuroglial potassium cycle during neurotransmission: role of Kir4.1 channels. PLoS Computational Biology. 2015; 11: e1004137. https://doi.org/10.1371/journal.pcbi.1004137.
[29] Zhu Y, Xu S, Eisenberg RS, Huang, H. Optic nerve microcirculation: Fluid flow and electrodiffusion. Physics of Fluids. 2021; 33: 041906. https://doi.org/10.1063/5.0046323.
[30] Kuffler SW, Nicholls JG, Orkand RK. Physiological properties of glial cells in the central nervous system of amphibia. Journal of Neurophysiology. 1966; 29: 768–787. https://doi.org/10.1152/jn.1966.29.4.768.
[31] Subileau M, Vittet D. Lymphatics in Eye Fluid Homeostasis: Minor Contributors or Significant Actors? Biology. 2021; 10: 582. https://doi.org/10.3390/biology10070582.
[32] Kedarasetti RT, Drew PJ, Costanzo F. Arterial vasodilation drives convective fluid flow in the brain: a poroelastic model. Fluids and Barriers of the CNS. 2022; 19: 34. https://doi.org/10.1186/s12987-022-00326-y.
[33] Nedergaard M, Goldman SA. Glymphatic failure as a final common pathway to dementia. Science (New York, N.Y.). 2020; 370: 50–56. https://doi.org/10.1126/science.abb8739.
[34] Olufunmilayo EO, Gerke-Duncan MB, Holsinger RMD. Oxidative Stress and Antioxidants in Neurodegenerative Disorders. Antioxidants (Basel, Switzerland). 2023; 12: 517. https://doi.org/10.3390/antiox12020517.
[35] Orfali R, Alwatban AZ, Orfali RS, Lau L, Chea N, Alotaibi AM, *et al*. Oxidative stress and ion channels in neurodegenerative diseases. Frontiers in Physiology. 2024; 15: 1320086. https://doi.org/10.3389/fphys.2024.1320086.
[36] Patel DC, Tewari BP, Chaunsali L, Sontheimer H. Neuron–glia interactions in the pathophysiology of epilepsy. Nature Reviews. Neuroscience. 2019; 20: 282–297. https://doi.org/10.1038/s41583-019-0126-4.
[37] Oksanen M, Lehtonen S, Jaronen M, Goldsteins G, Hämäläinen RH, Koistinaho J. Astrocyte alterations in neurodegenerative pathologies and their modeling in human induced pluripotent stem cell platforms. Cellular and Molecular Life Sciences: CMLS. 2019; 76: 2739–2760. https://doi.org/10.1007/s00018-019-03111-7.